Effects of structural parameters on flow boiling performance of reentrant porous microchannels

2014 J. Micromech. Microeng. 24 065025

(http://iopscience.iop.org/0960-1317/24/6/065025)

IOP Publishing Journal of Micromechanics and Microengineering
J. Micromech. Microeng. **24** (2014) 065025 (14pp) doi:10.1088/0960-1317/24/6/065025

Effects of structural parameters on flow boiling performance of reentrant porous microchannels

Daxiang Deng[1,3], Yong Tang[2], Haoran Shao[2], Jian Zeng[2], Wei Zhou[1] and Dejie Liang[2]

[1] Department of Mechanical and Electrical Engineering, Xiamen University, Xiamen, 361005, People's Republic of China
[2] Key Laboratory of Surface Functional Structure Manufacturing of Guangdong High Education Institutes, School of Mechanical and Automotive Engineering, South China University of Technology, Guangzhou 510640, People's Republic of China

E-mail: dengdaxiang88@gmail.com

Received 15 January 2014, revised 3 April 2014
Accepted for publication 29 April 2014
Published 19 May 2014

Abstract

Flow boiling within advanced microchannel heat sinks provides an efficient and attractive method for the cooling of microelectronics chips. In this study, a series of porous microchannels with Ω-shaped reentrant configurations were developed for application in heat sink cooling. The reentrant porous microchannels were fabricated by using a solid-state sintering method under the replication of specially designed sintering modules. Micro wire electrical discharge machining was utilized to process the graphite-based sintering modules. Two types of commonly used copper powder in heat transfer devices, i.e., spherical and irregular powder, with three fractions of particle sizes respectively, were utilized to construct the porous microchannel heat sinks. The effects of powder type and size on the flow boiling performance of reentrant porous microchannels, i.e., two-phase heat transfer, pressure drop and flow instabilities, were examined under boiling deionized water conditions. The test results show that enhanced two-phase heat transfer was achieved with the increase of particle size for the reentrant porous microchannels with spherical powder, while the reversed trend existed for the counterparts with irregular powder. The reentrant porous microchannels with irregular powder of the smallest particle size presented the best heat transfer performance and lowest pressure drop.

Keywords: porous microchannels, reentrant, flow boiling, microchannel heat sink

(Some figures may appear in colour only in the online journal)

Nomenclature

A_{ch}	total heat transfer area of microchannels, m^2
A_t	platform area of copper block, m^2
d	powder particle diameter, μm
D_h	hydraulic diameter, mm
H_{slot}	height of slot, mm
h_{fg}	latent heat of vaporization, kJ kg^{-1}
h_{tp}	local two-phase heat transfer coefficient, kW m^{-2} K
k_{Cu}	thermal conductivity of copper block, W m^{-1} K
k_{por}	thermal conductivity of reentrant porous microchannels, W m^{-1} K
K_s	thermal conductivity of solder, W m^{-1} K
L	length of heat sink, mm
L_i	distance from the inlet to thermocouple location in the stream-wise direction, m
l_{Cu}	distance between the thermocouple and the top surface of copper block, m
l_{hs}	distance between heat sink bottom surface and the bottom of circular portion of reentrant cavity, m
m	fin parameter

[3] Author to whom any correspondence should be addressed.

$\dot{m}$	mass flow rate (kg s^{-1})
N	number of reentrant microchannels
ONB	onset of nucleation boiling
P_{cir}	perimeter of circular portion of reentrant microchannel, m
q_{eff}	effective heat power, W
Q	total power input, W
q''_{eff}	effective heat flux based on platform area, kW m^{-2}
Ra	center-line average roughness, μm
R_z	peak-to-valley roughness, μm
T_{tci}	thermocouple reading ($i = 1$–5), °C
T_{in}	inlet fluid temperature, °C
$T_{w,tci}$	channel bottom wall temperature at thermocouple location, °C
$\Delta T_{sct,tci}$	wall superheat, °C
ΔP	pressure drop, kPa
ΔP_c	inlet contraction pressure drop, kPa
ΔP_e	outlet expansion pressure drop, kPa
$T_{sat,\,tci}$	local saturation temperature of thermocouple location, °C
W	width of heat sink, mm
W_{fin}	width of fin between two reentrant microchannels, mm
x	thermodynamic quality

Greek symbols

ε	porosity
η	fin efficiency
ρ	density of fluid, kg m^{-3}

Subscripts

cir	circular portion
Cu	copper
hs	heat sink
fin	fin
tci	thermocouple location
in	inlet
por	porous
sat	saturation
slot	slot
s	solder
tp	two-phase

1. Introduction

With their capacity to dissipate a large amount of heat from compact high-heat-flux micro devices, microchannel heat sinks have been extensively regarded to be an attractive choice for the cooling of microelectronic and military systems [1, 2]. To date, silicon microchannel heat sinks [3–5] have been widely explored due to their good compatibility with integrated chips. However, it is a tedious and costly procedure to process silicon microchannels using the etching method, because the silicon material results in poor thermal and mechanical properties [6]. While for the other solid microchannels heat sinks to explore the above merits further, i.e., copper or aluminum metal microchannel heat sinks [7, 8], despite their good thermal conductivities, the large wall superheat used to trigger the flow boiling in microchannels may be problematic for the safe operation of microchannel heat sink cooling systems. To address this issue, researchers have attempted to develop more sophisticated methods, such as adding sprayed ABM coating [9], nanotube coating [10], diffusion-brazed wire mesh coating [11] or sintered porous powder coating [12] on the bottom wall of the microchannels. Since the introduction of porous coating facilitates a significant increase of nucleation site densities, a notable extension of surface area, as well as the capillary-assistance for keeping the surface wetted, enhanced flow boiling heat transfer has been reached in such microchannel heat sinks. Furthermore, porous material-based microchannels, other than just adding a porous layer on the solid microchannel bottom surface, have been recently proposed for constructing heat sinks to explore the above merits further. Hakamada *et al* [13] developed a type of copper powder-based metallic microchannel using the spacer method, in which aluminum wire spacers were replicated after sintering them together with the compaction of the copper powder base. Cora [14, 15] fabricated porous copper powder-based V-shaped microchannels utilizing two kinds of warm compaction methods, i.e., compacted then sintered and sintered then compacted. Pool boiling tests results showed that these porous microchannels enhanced the critical heat flux (CHF) significantly.

Besides the aforementioned porous methods, reentrant cavities have been widely known to promote the boiling nucleation as a vapor trap since the pioneering work by Benjamin and Westwater in 1961 [16]. The superior performance of reentrant cavities in pool boiling systems has been demonstrated repeatedly [17, 18], and its implementation in the outer finned tubes of heat exchangers promoted the third-generation heat transfer enhancement in industry [19]. The merits of reentrant cavities have been also extended to microchannel heat sinks, such as the reentrant cavity silicon heat sink by Goyal *et al* [20], Boer *et al* [21] using buried channel technology, and the rectangular silicon microchannels with reentrant cavities on the side wall by Peles *et al* [22]. However, all of the above microchannels were fabricated by complicated and costly MEMS procedures, as the fabrication difficulties for the reentrant configurations may increase significantly as compared to those of open microchannels. In view of this, a different method was proposed to process the reentrant microchannels by Deng *et al* [23], i.e., a novel kind of reentrant porous powder microchannel has been preliminarily developed using the solid-state sintering method. By the replication of the convex configurations of a Ω-shaped module, the reentrant porous microchannels were easily fabricated with low cost. Flow boiling tests have demonstrated a drastic decrease of wall superheat for onset of nucleate boiling (ONB), a significant enhancement of flow boiling heat transfer and mitigation of two-phase flow instabilities compared to solid copper microchannels with the same reentrant configurations.

In the boiling systems of porous coating surfaces, the structural parameters of the porous base, such as the porous particle shapes and sizes, played a vital role on the heat transfer

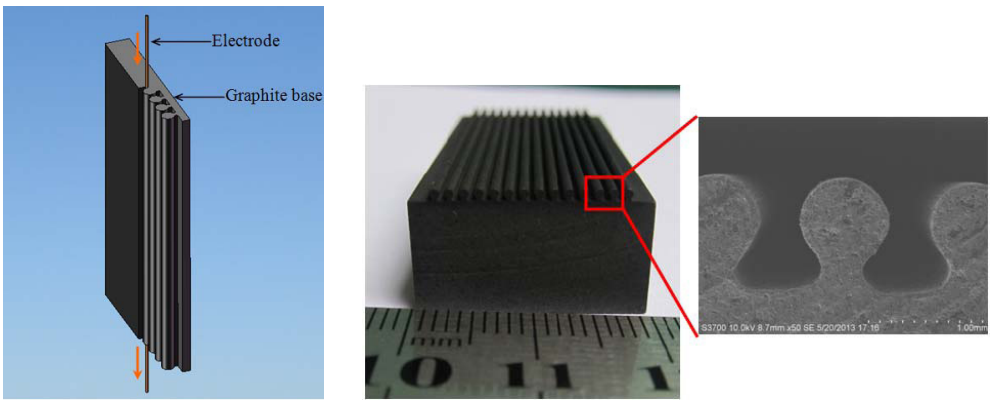

(*a*) (*b*)

Figure 1. Fabrication of the graphite Ω-shaped mold. (*a*) EDM fabrication, (*b*) final Ω-shaped mold.

performance, which has been demonstrated repeatedly in pool boiling systems, such as those by Cora *et al* [14], Wu *et al* [24], Weibel *et al* [25] and Hong *et al* [26]. Such structural effects have also been highlighted in the flow boiling of heat sinks with porous coating. Peterson and Chang [27] examined the two-phase heat transfer performance of a rectangular channel filled with various sintered copper powder sizes (0.97, 0.54, 0.39, and 0.33 mm). It was demonstrated that the porous channels comprised of smaller diameter spheres presented a larger heat transfer coefficient because of their larger heat transfer area. However, the experimental results of a single small copper rectangular channel with sintered copper porous coatings by Sun *et al* [12, 28] revealed that there was an optimum medium spherical copper particle size to reach the maximum heat transfer performance, which was true for two liquid tests (water [12], FC-72 [28]) and two sets of particle sizes. Similar results were found in the flow boiling tests of ethanol in parallel rectangular microchannels with sintered dendrite copper powder coatings by Bai *et al* [29], in which three average particle sizes of 30, 55, and 90 μm were utilized and the medium one exhibited the best heat transfer performance. In addition, Sarwar *et al* [30] found that the critical heat flux (CHF) of water flow boiling in steel tubes with painted Al_2O_3 nano-porous coatings can be improved by using coatings with larger micro-particles. As enumerated above, the current efforts were all devoted to solid metal-based channels with porous coatings on the channel surface. However, to the best of the authors' knowledge, the effects of structural parameters on the flow boiling behavior of porous-based microchannels heat sinks have not yet been understood. Such studies are required to provide critical information for the design optimization as well as the fabrication and implementation of porous microchannel heat sinks.

In the present study, the influences of structural parameters on the flow boiling performance of reentrant porous microchannels are explored. It is aimed to provide the critical information for the design optimization of such porous microchannel heat sinks, which favors for the efficient cooling of high-heat-flux microelectronic devices. Meanwhile, an in-depth insight into the fabrication process of the reentrant porous microchannels is also provided.

2. Fabrication of reentrant porous microchannels

2.1. Preparation of the sintering replication module

The porous microchannels with reentrant configurations were fabricated by using a solid-state sintering method. The most critical part of the processing procedure was the fabrication of the sintering module, as the reentrant configuration was replicated by a convex Ω-shaped module. In the preliminary trials, two common materials, i.e., stainless steel and graphite, were utilized to process the sintering module. They were both fabricated to the convex Ω shape by using micro wire electrical discharge machining (EDM). Due to the good metal hardness, stainless steel was easy to process into the complex shape by EDM wire cut. However, when the stainless steel was utilized as the sintering module, it was found that the sintered copper powder matrix was too hard to demold from the convex module, as the adhesion force between the copper particles and the stainless steel surface was so large that they were hard to separate from each other after the high temperature sintering, especially when the length of the porous microchannels was as long as 45 mm. On the other side, though the graphite was of poor hardness, which was unfavorable for the EDM process, the convex Ω shape was successfully formed on the graphite plate by carefully choosing the processing parameters. A molybdenum electrode with diameter of 100 μm was utilized; multipass cut with low speed was performed in the wire cut process, and the machining parameters were also optimized after several trials as follows: pulse width of 6 μs, pulse interval of 60 μs, short-circuit current of 2.5 A, open-circuit voltage of 105 V, and wire speed of 5.2 mm^2 min^{-1}. The fabricated graphite mold is shown in figure 1. Since the graphite was inactive with copper powders at high sintering temperatures, and the carbon material of the graphite module surface can serve as a lubrication layer, it can facilitate the demolding of porous microchannels from the convex Ω-shaped mold. Therefore, the graphite mold was finally chosen for the solid-state sintering.

2.2. Sintering and demolding

The porous microchannel matrix was fabricated by the solid-state sintering of copper powder on top of the graphite mold,

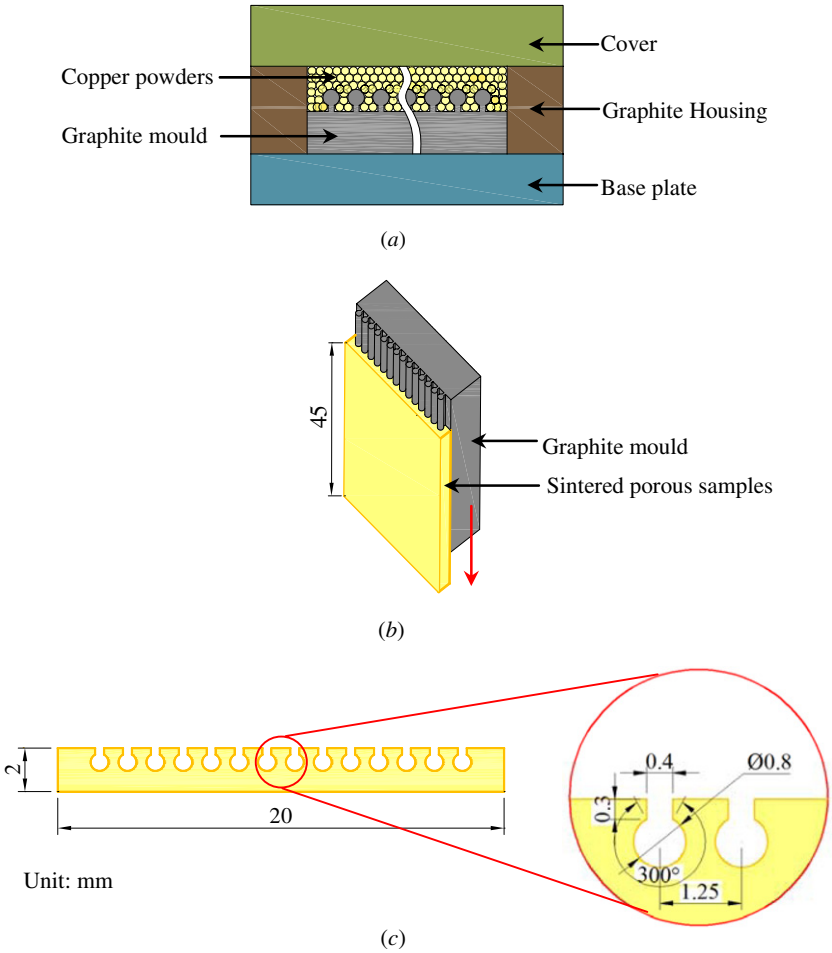

Figure 2. Schematic of the sintering and demolding process of reentrant sintered porous microchannels. (*a*) Power filling and sintering, (*b*) demolding, (*c*) final reentrant porous microchannels.

as depicted in figure 2. Firstly, the graphite mold was located in the center of graphite housing. There was a gap between the height of the mold and the top surface of the housing, which was designed to form the base of the porous channels with a given thickness after filling copper powder to the top surface level of the graphite housing. A cover and base plate were also used to ensure that the backside of the sintered porous channels was flat, which plays a critical role in minimizing the thermal resistance between the heat source and porous microchannels. It should be pointed out that no pressure was applied on the cover plate, and the loose sintering method was utilized to maximize the porosity of the final porous channel matrix. Subsequently, the assembly was sintered in a box-type furnace with a programmable temperature controller for 30–60 min at 950 $\pm$ 10 °C. We used the stage heating method to optimize the heating rate in the sintering process. When the temperature was below 850 °C, the heating rate was kept at 300 °C h^{-1}; and when the temperature was above 850 °C, the heating rate was reduced to 200 °C h^{-1}. The furnace chamber was purged by nitrogen to get rid of the air and then filled with hydrogen to maintain a reductive atmosphere. The pressure of the hydrogen in the furnace chamber was kept at 0.15 MPa. After the sintering was complete, the assembly was taken out and cooled to room temperature.

During the demolding procedure, care should be taken to force the porous matrix with reentrant microchannels to separate from the convex mold. Intermittent pushing force was applied on the base part of the cross-section area of porous matrix, by which the porous microchannels were pushed out from the graphite mold little by little. Thanks to no adhesion between the copper particle and graphite, the porous reentrant microchannels were finally separated from the graphite mold.

In the present study, two kinds of commercial copper powder of purity over 99.5% were employed with all the sizes smaller than 150 μm, the range of which are normally used in two-phase heat transfer devices such as two-phase heat sinks [28, 29] and heat pipes [26]. One kind is of the irregular morphology produced by water atomization, and the other is the spherical type produced by gas atomization. For the purpose of design optimization, the two kinds of powder were sieved into four fractions: <50, 50–75, 75–110 and 110–150 μm. However, for the powder of the smallest size <50 μm, the small particles bonded together very firmly, as their tiny surface area facilitated the accumulation between adjacent particles and formation of particle clusters under high temperature sintering, and the adhesion force between the particles and the graphite mold increased significantly. Considering the convex Ω shape and the pool strength of the

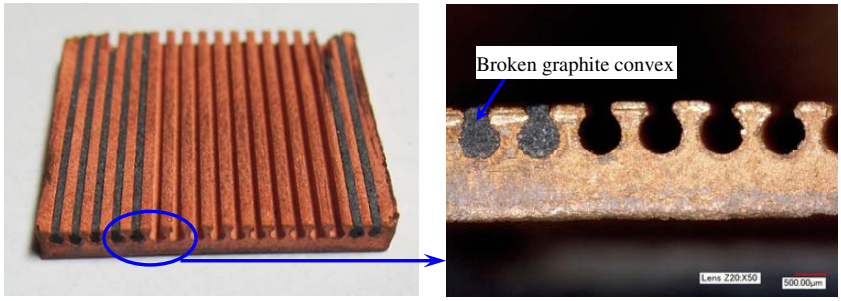

Figure 3. Illustration of the failed demolding samples with the spherical powder of <50 μm.

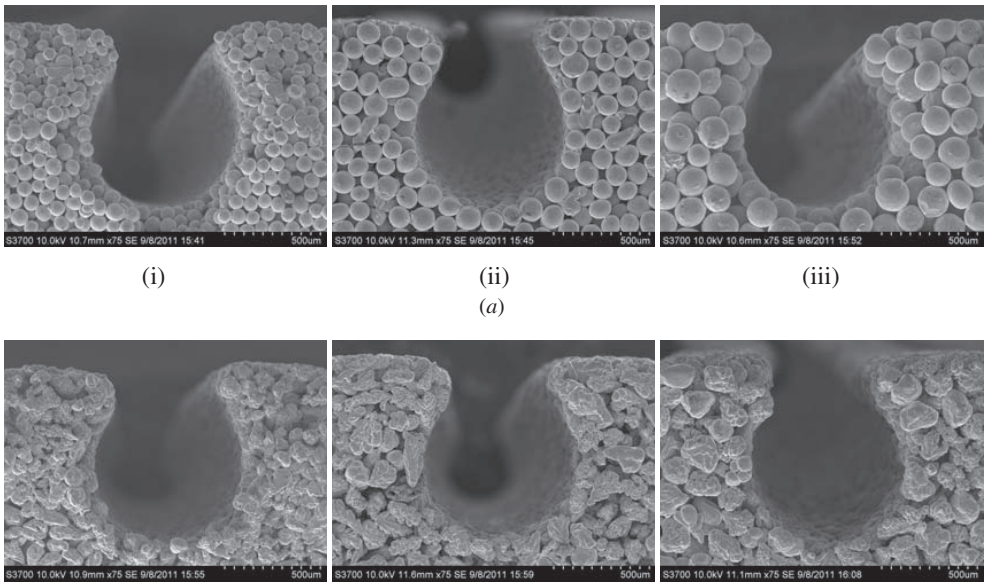

Figure 4. SEM images of the six reentrant porous microchannels samples with (*a*) spherical powder, (*b*) irregular powder. (i) RPM-S1; (ii) RPM-S2; (iii) RPM-S3; (iv) RPM-I1; (v) RPM-I2; (vi) RPM-I3.

Table 1. Specification of reentrant porous microchannels samples.

Sample	Powder type	Powder particle size, d (μm)	Dimension, $W \times H \times L$ (mm)	Hydraulic diameter, D_h (μm)	Porosity of porous matrix, ε
RPM-S1	Spherical	50–75	20 × 2 × 45	775	0.39
RPM-S2	Spherical	75–110	20 × 2 × 45	786	0.39
RPM-S3	Spherical	110–150	20 × 2 × 45	782	0.39
RPM-I1	Irregular	50–75	20 × 2 × 45	792	0.39
RPM-I2	Irregular	75–110	20 × 2 × 45	798	0.39
RPM-I3	Irregular	110–150	20 × 2 × 45	782	0.39

graphite mold, it was found during repeated trials that some of the graphite convex broke down from the mold during the demolding process, as illustrated in figure 3. For other samples with three large particle sizes, the decrease of the contact between particles and the mold surface and the increase of large pores in the porous matrix resulted in much smaller adhesion forces than that of <50 μm particles. They were easy to demold from the graphite mold and no cracks in graphite module occurred. Besides, due to the good strength of sintered copper powder matrix and the large flat top surface of the microchannels, it was found that the reentrant porous microchannels were strong enough to assemble with screws in the test section, as described in the subsequent section, and no cracks in the porous wall occurred during repeated tests. They were then utilized for tests in the flow boiling systems, as described in the following sections. Figure 4 shows SEM images of the reentrant porous microchannels with both powder types and three particle sizes, i.e., 50–75, 75–110 and 110–150 μm, respectively. The parameters of these six samples are listed in table 1.

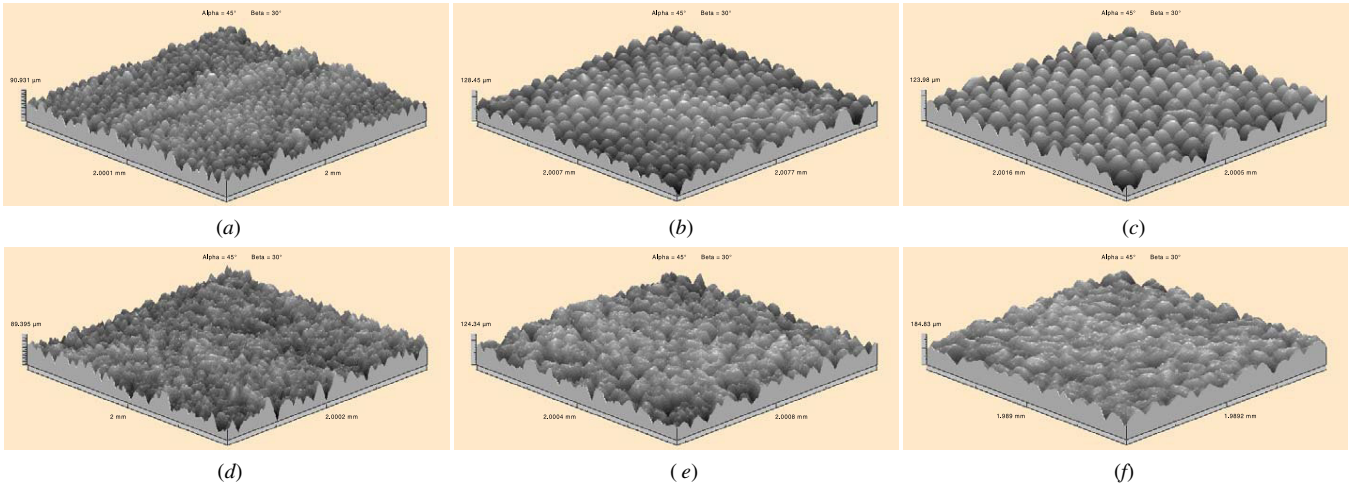

Figure 5. Surface profiles of the six reentrant porous microchannels samples. (*a*) RPM-S1; (*b*) RPM-S2; (*c*) RPM-S3; (*d*) RPM-I1; (*e*) RPM-I2; (*f*) RPM-I3.

Table 2. Surface roughness measurement of porous matrix of the reentrant porous microchannels.

Sample	R_a, μm	R_z, μm
RPM-S1	8.5	46.8
RPM-S2	9.9	49.1
RPM-S3	11.9	59.9
RPM-I1	8.4	51.8
RPM-I2	11.5	59.8
RPM-I3	10.3	56.7

2.3. Characterizations of the surface roughness of the porous channel

The surface roughness of the porous reentrant microchannels was measured using a surface profilometer (Talysurf CLI 1000, Taylor Hobson precision Corp., USA). Three areas of the flat surface of the porous channels were randomly selected and measured on each sample, and these three values of the center-line average roughness (R_a) and peak-to-valley roughness (R_z) were averaged. The surface profiles of the six samples are shown in figure 5. Table 2 summarizes the measured roughness of porous matrix for these samples. One can note that it exhibits a larger roughness with an increase of particle size for the porous samples with spherical powder, as there were more distinctive peaks and valleys among the porous matrix with the larger particle size. However, this monotonic increase in roughness was not true for those with irregular powder, which was attributed to the special topography of irregular powder. The surface roughness of porous channels was larger than the copper metal microchannels fabricated by the EDM process, e.g., 3.9 and 6.7 μm in the work of Jones and Garimella [31]. They were much larger than the silicon microchannels fabricated by the etching method, which were normally below 1 μm [32]. This large surface roughness as well as the tiny pores may facilitate nucleate boiling, which will be discussed later.

3. Flow boiling experiments

3.1. Experimental setup

The experimental setup, as shown in figure 6, consists of a liquid circulation system (including a water tank, a magnetic gear pump, a 7 μm filter and valves), a micro turbine type flowmeter, inlet temperature adjusting parts (constant temperature water bath and heat exchanger), a test section and heating module, a flow visualization system, and a data acquisition system. Deionized water, which was fully degassed before each experiment run, was utilized as the working fluid. The test section, as shown in figure 7, was composed of the sintered porous microchannels sample, inlet and outlet plenums, a Pyrex 7740 glass cover plate, fiberglass flow housing, a copper block heating module and insulating components. All six porous microchannel samples were 45 mm long, 20 mm wide and 2 mm high, and contained 14 parallel reentrant microchannels. The geometry of the sample is shown in figure 2(*c*). It was soldered on top of the copper block heat module using a 0.1 mm thick layer of solder (Pb-Sn-Ag-Sb, $k_s = 50$ W m$^{-1} \cdot$ K^{-1}). The top surface dimension of the copper block was the same as the base of the microchannel sample. Four slots were cut along the height direction of the copper block to reduce heat spread within the copper block and supply more uniform heat flux distribution. The copper block was heated by ten cartridge heaters with a maximum total power of 1000 W. Five type-K thermocouples were embedded in the copper block at a location 1.8 mm under the heating surface to measure the wall temperature distribution in the flow direction. The interval between each thermocouple was 10 mm, and the first and last thermocouples were located at a distance of 2.5 mm to the inlet or outlet plenum. Horizontal inlet and outlet manifold arrangements were utilized for the liquid flow, and no deep inlet and outlet reservoirs were adopted to reduce the compressive upstream volume. Pressure port spaces were left in the inlet and outlet plenum for the measurement of inlet/outlet pressure by two pressure transducers with a response time of 3 ms. Two type-K thermocouples were set at about 5 mm before or after the

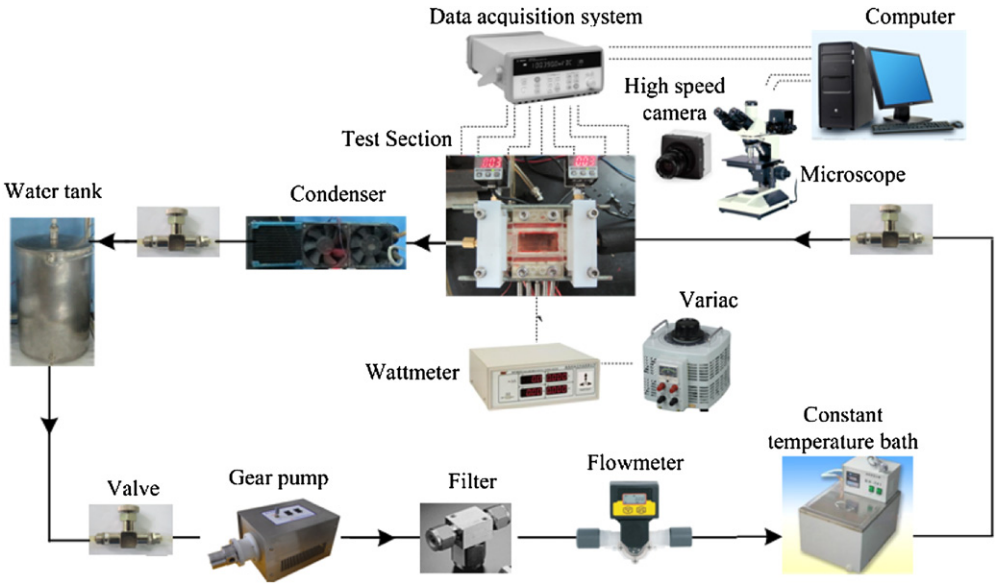

Figure 6. Schematic of the flow boiling test system.

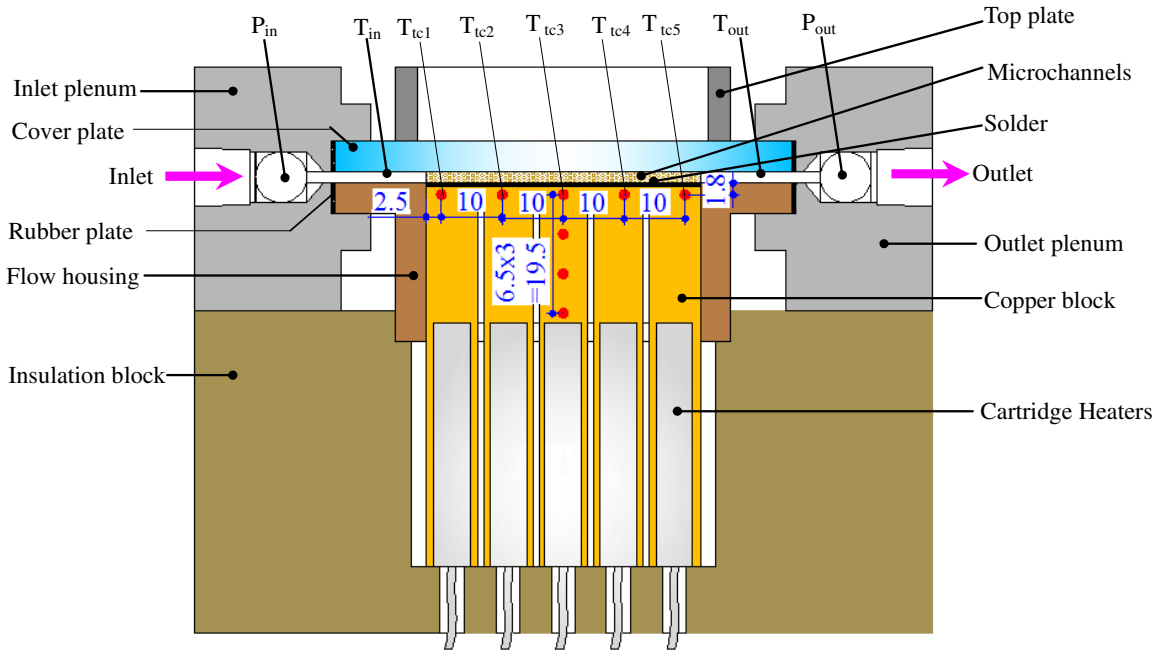

Figure 7. Schematic of the cross-section of the test section.

microchannel sample to measure the inlet/outlet temperature. The pressure at the outlet plenum is estimated to be about 1 atm as the loop was open to the ambient air. A Bakelite insulating block, in which the bottom part of the copper block was located, was used to ensure insulation and support for the flow housing. Moreover, to minimize heat loss, the assembly of the test section was insulated with glass fiber, except for the top surface for flow visualization. Flow visualization was conducted using a microscope and a high-speed camera (Fastec HiSpec DVR 2F), and the frame rate was typically set at 500–1000 frame s^{-1} for the test samples.

In the present study, all the porous microchannel samples were tested under an inlet temperature of 90 °C, namely, the subcooling of 10 °C. The flow rate was the same for all samples for ease of comparison. The electrical power was supplied by the variac to the test section in small increments of 15–30 W. All measurements of temperature and pressure were collected at steady-state with 1s intervals for 2 min.

3.2. Data reduction

Mass flux is referred to as G and defined as

$$G = \dot{V}\rho/A_c \tag{1}$$

in which $\dot{V}$ is the volumetric flow rate, ρ is the fluid density, A_c is the cross-section area of the microchannels.

The efficient heat flux was given by

$$q''_{\text{eff}} = q_{\text{eff}}/A_t \tag{2}$$

in which A_t is the top platform area of the copper block, $q_{\text{eff}} = \varphi Q/A_t$, where Q is the total heating power, φ is the heat transfer ratio, which is defined as the effective enthalpy increment across the test section divided by the total heating power. φ was determined from a set of single-phase heat transfer experiments prior to boiling tests. In the present study, it was found to be in the range of 0.76–0.84. Therefore, the average value of 0.8 was used to calculate the efficient heat flux.

The boiling heat transfer coefficient (h_{tp}) was calculated as follows,

$$h_{\text{tp,tci}} = \frac{q_{\text{eff}}}{\Delta T_{\text{sat,tci}} A_{\text{ch}}} \tag{3}$$

and

$$\Delta T_{\text{sat,tci}} = T_{w,\text{tci}} - T_{\text{sat,tci}} \tag{4}$$

where,

$$T_{w,\text{tci}} = T_{\text{tci}} - q_{\text{eff}} \left(\frac{l_{\text{Cu}}}{k_{\text{Cu}} A_t} + \frac{l_{hs}}{k_{\text{por}} A_t} + \frac{t_s}{k_s A_t} \right) \tag{5}$$

where $\Delta T_{\text{sat,tci}}$ is the local wall superheat, $T_{\text{sat,tci}}$ is the liquid saturation temperature. The wall temperature of the porous microchannel ($T_{w,\text{tci}}$) was deduced from a thermal resistance network (see [23] for details). The thermal conductivities of porous matrix, k_{por}, were determined separately. Sintered porous specimens were prepared using identical copper powder and fabrication parameters as the present porous microchannels, and their porosities were the same as the porous microchannels. Instead these specimens were measured using the steady-state axial heat flow technique in dry conditions, which were conducted in a standard thermophysical property test system (Quantum Design Model PPMS-9). Though there may be small discrepancies between such measurements and the working conditions of reentrant porous microchannels, it is believed this can be thought to be negligible as the penetration of water into porous matrix were very limited as the permeability of porous matrix were in the order of 10^{-12} m^2 [23]. The k_{por} of these samples with two kinds of copper powder ranged from 39–48 W m^{-1} · K^{-1}, the differences of which were small and have negligible effects on the thermal resistance of different porous microchannels. A_{ch} is the total heat transfer area of reentrant microchannels, which is given by the fin analysis method as follows,

$$A_{\text{ch}} = NL\left(P_{\text{cir}} + 2\eta H_{\text{slot}}\right) \tag{6}$$

where P_{cir} is the perimeter of the circular portion of each reentrant microchannel, H_{slot} is the height of the slot, N is the total number of reentrant microchannels, η is the fin efficiency as given by

$$\eta = \frac{\tanh\left(mH_{\text{slot}}\right)}{mH_{\text{slot}}} \tag{7}$$

where m is the fin parameter, given by

$$m = \sqrt{\frac{h_{\text{tp,tci}} \cdot 2\left(L + W_{\text{fin}}\right)}{k_{hs} L W_{\text{fin}}}} \tag{8}$$

where W_{fin} is the width of the fin between two adjacent reentrant microchannels. h_{tp} can thus be evaluated employing equations (3) and (6)–(8) with an iterative scheme.

The mass quality can be obtained as follows,

$$x = \frac{1}{h_{fg}} \left(\frac{q_{\text{eff}}}{\dot{m}} \cdot \frac{L_i}{L} - C_p \left(T_{\text{sat,tci}} - T_{\text{in}} \right) \right)$$

where h_{fg} is the latent heat of vaporization, L_{i} is the distance from the inlet to the thermocouple location.

The pressure drop across the microchannels was calculated as follows,

$$\Delta P = \left(P_{\text{in}} - \Delta P_c\right) - \left(P_{\text{out}} + \Delta P_e\right)$$

where ΔP_c denotes the inlet contraction pressure drop and ΔP_e is the outlet expansion pressure loss. They were estimated by the method detailed in Qu and Mudawar [33], and were found to be only 1–5% of the total measured pressure drops, which can be thought to be negligible. The obtained pressure drop ΔP consisted of the one in the single-phase flow region and the two-phase flow pressure drop including the accelerational and frictional loss terms [33].

Uncertainties in individual temperature measurements are ± 0.3 °C for the type-K thermocouples. The measurement errors for the flow meter and pressure transducer are 2% and 0.1% of full scale, respectively. The uncertainty associated with the heat flux measurement is estimated to be 1%. The uncertainties in the microchannel geometry dimension were found to range from the smallest 7.6% to the largest 9.2%. A standard error analysis method [34] revealed that the uncertainties in the vapor quality and two-phase heat transfer coefficient were in the range of 12.2–14.1%, 14.4–16.8%.

4. Results and discussion

4.1. Boiling curves

Figure 8 shows the boiling curves of six porous microchannels at the same operation condition ($G = 200$ kg m^{-2} s^{-1}, $T_{\text{in}} = 90$ °C). We focused on the local wall temperature overshoot on the downstream thermocouple location near the exit (Z_{tc5}). At low heat fluxes, single-phase forced convection dominates in the porous microchannels, and the wall superheat increases quickly with a small heat flux increment. Boiling was initiated with the heat flux increasing, where there is a radical change in the slope of the curve q''_{eff}–ΔT_{sat}, indicating the ONB. It can be noted that all the porous microchannels samples can trigger ONB at a very small wall temperature overshoot, i.e., smaller than 1.5 °C. This was much smaller than that of other copper and silicon microchannels [35, 36] thanks to the significant increase of nucleation sites supplied by the porous matrix.

4.2. Flow boiling heat transfer performance

In the present study, as the two-phase flow boiling was conducted at a small inlet subcooling (10 °C), the flow boiling of six porous microchannels samples was mostly in the saturated boiling region, therefore the saturated boiling performances were accessed. Figure 9 illustrates the local heat transfer coefficient of the most downstream thermocouple location (Z_{tc5}) as a function of vapor quality. At the initial stage of saturated boiling, all the samples presented a large h_{tp}. The microscopic pores formed between adjacent particles in the

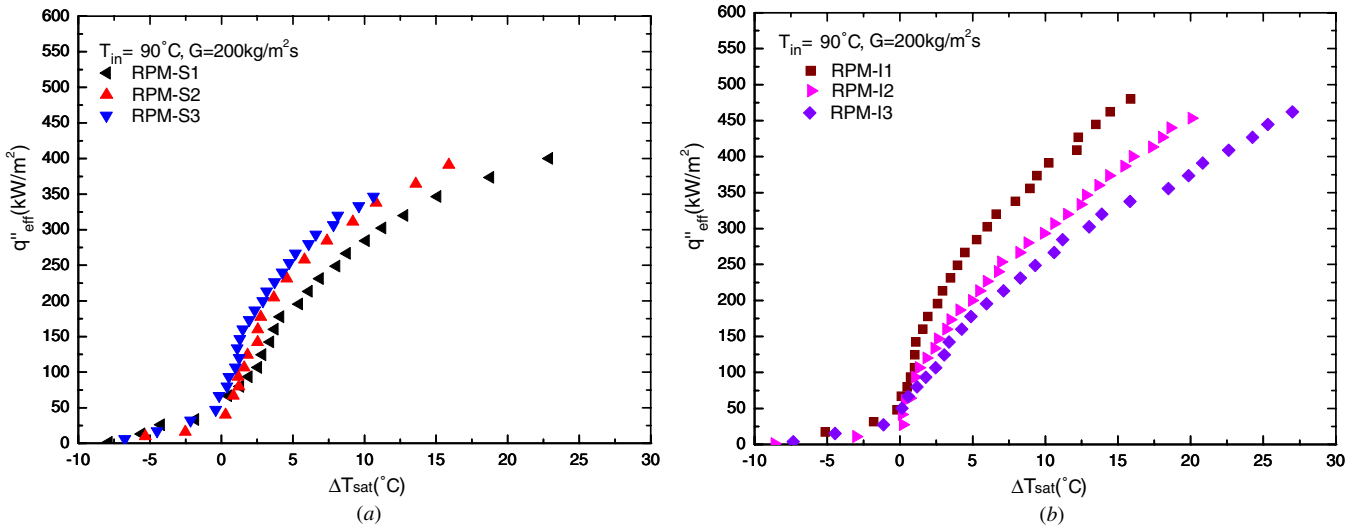

Figure 8. Boiling curves of the reentrant porous microchannels at $G = 200$ kg m^{-2}·s^{-1} and $T_{in} = 90$ °C: (*a*) spherical powder samples; (*b*) irregular powder samples.

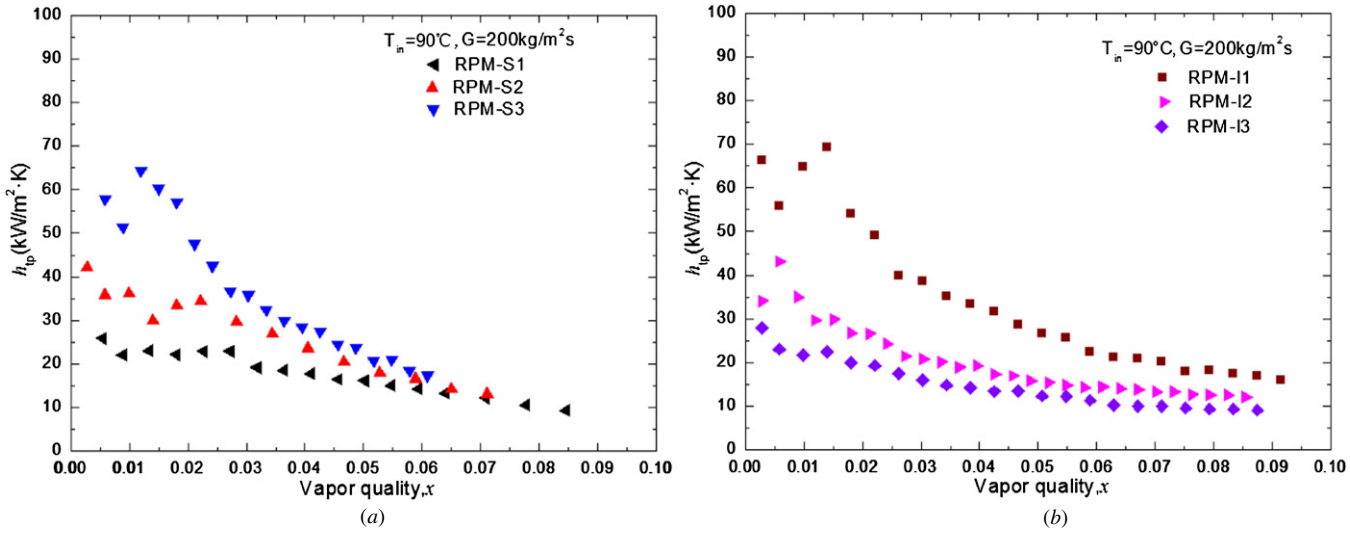

Figure 9. Two-phase heat transfer performance of the reentrant porous microchannels: (*a*) spherical powder samples; (*b*) irregular powder samples.

porous matrix wall provided lots of tiny cavities for bubble embryos, which served as stable nucleate sites. A large amount of nucleate sites were activated once the boiling commenced, and induced a large bubble growth and departure frequency. Latent heat was released quickly, and resulted in a large h_{tp}. Following the finding of our previous study [23], this stage was linked to the nucleate boiling dominant region. With the increase of heat flux as well as vapor quality, the two-phase heat transfer coefficient tended to decrease, implying that the boiling mechanism may change. A transition from nucleate boiling to forced convective boiling occurred as the increase of heat flux played an adverse role on the h_{tp}, and the heat transfer performance was strongly dependent on vapor quality. Annular flow was found to be the dominant flow pattern in porous microchannels with both spherical and irregular powders, as illustrated in figure 10. Nucleate boiling was suppressed at moderate to high heat fluxes, and the heat was mainly dissipated by the thin film evaporation between the vapor core and the microchannel wall. The same trend was also observed in the flow boiling of rectangular microchannels with porous coatings on the bottom surface [28], as well as in the solid copper or silicon rectangular microchannels under the water boiling conditions [22, 35].

For the porous reentrant microchannels with spherical powders, one can note from figure 9(*a*) that superior heat transfer performance can be reached with the increase of powder size, which was especially pronounced at small heat flux and vapor quality. There were notable differences of h_{tp} at the initial boiling region, indicating that the particle size of spherical powder played a significant role on the h_{tp} at this stage. As aforementioned, the nucleate boiling governed the two-phase heat transfer at small heat flux and vapor quality. The number and geometry of nucleate sites introduced by porous matrix determined the boiling heat transfer performance. From the microscope images of the porous wall of three samples, as presented in figure 11, it

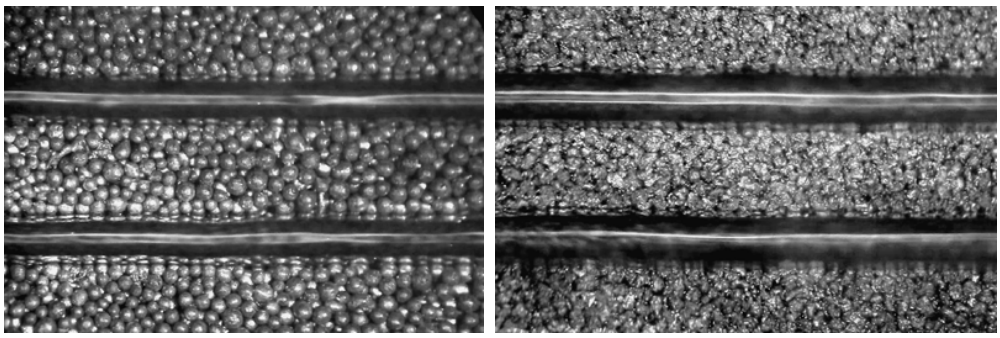

(*a*) (*b*)

Figure 10. Annular flow in two kinds of reentrant porous microchannels: (*a*) spherical powder sample RPM-S2 at $T_{in} = 90\ ^{\circ}C$, $G = 200\ kg\ m^{-2}{\cdot}s^{-1}$, $q''_{eff} = 364\ kW\ m^{-2}$; (*b*) irregular powder sample RPM-I2 at $T_{in} = 90\ ^{\circ}C$, $G = 200\ kg\ m^{-2}{\cdot}s^{-1}$, $q''_{eff} = 373\ kW\ m^{-2}$.

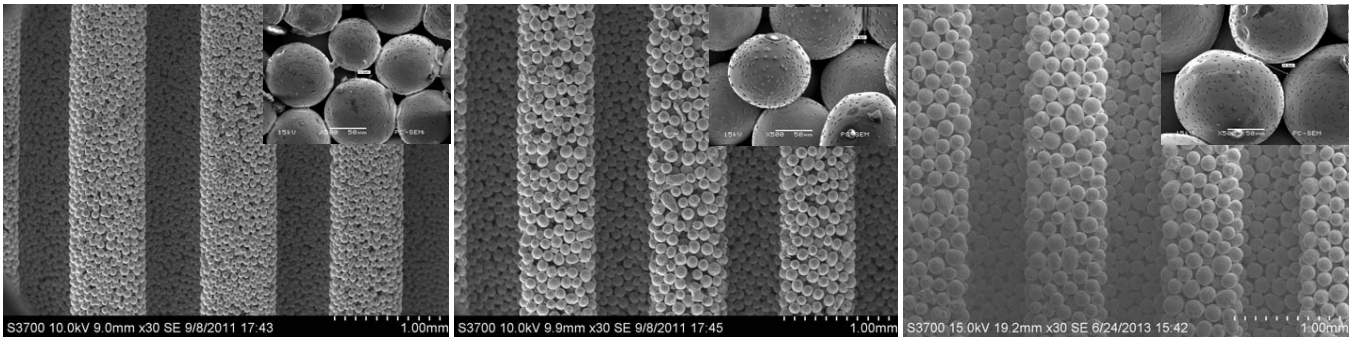

(*a*) (*b*) (*c*)

Figure 11. SEM images of the top view of the three reentrant porous microchannels with spherical powder. The microscope pictures were also inserted in each picture. (*a*) RPM-S1, (*b*) RPM-S2, (*c*) RPM-S3.

can be noted that more open and large pores formed easily in the sample with a large particle size. Due to its large surface area of large powder, it was hard to form the sintering necks between adjacent particles during the sintering process, as the driving force needed for enough mass propagation at the joint point of adjacent particles was too large. As such, the porous matrix with large size of powder provided a huge number of opening pores and they were apt to interconnect with adjacent ones, therefore it facilitated the bubble outflow and successive liquid replenishment. Stable nucleation sites were maintained easily, which promoted the heat transfer performance. On the other side, though there may have been more tiny pores in the matrix of the sample RPM-S1 as compared to the other two samples, these pores tended to close due the much easier sintering bonding in the sintering process. This can be also found in the topography images in figure 5. It hinders the liquid penetration into the microscopic pores of the microchannel wall, and also introduces large resistance for the growth and removal of vapor bubbles. Therefore, it was unfavorable for the boiling nucleation. At moderate to high heat fluxes, the h_{tp} of three porous microchannels with spherical powders changed to become close, indicating that the effects of spherical particle size on the h_{tp} tended to diminish with the increase of heat flux and vapor quality. At this stage, nucleate boiling was intensely suppressed and thin film evaporation governed the heat transfer of microchannels. It seems that the spherical powder size may exert a negligible influence on the thin film evaporation.

On the other side, for the three porous samples with irregular powders, the particle size played an adverse role on the two-phase heat transfer performance as compared to those with spherical powders, i.e., with the increase of particle size, the porous microchannels presented an decreasing trend in h_{tp}. Obvious differences of h_{tp} can be also found at small heat flux and vapor quality, which can be related to the nucleation characteristics introduced by the different porous matrix with irregular powder. Unlike the spherical powder, it was hard to form close pores in the irregular porous microchannel walls due to the irregular shape of the powder, as illustrated in figure 12. The large surface area and special shape of irregular particles facilitated the formation of numerous interconnected cavities and gaps. The cavities between adjacent powders served as bubble embryos, and the gaps supplied paths for the vapor bubble growth and removal. The number of these cavities and gaps increased with the decrease of powder size, which promoted the nucleate site densities when the nucleate boiling initiated. Enhanced two-phase heat transfer performance can thus be expected for the sample with smaller irregular powder size. With the increase of heat flux and vapor quality, the difference in h_{tp} of three irregular powder samples was also found to decrease, but did not diminish in the same way as the aforementioned spherical samples. Since the thin film evaporation dominated at this period, the film thickness may be altered by different wall topographies of the irregular powder porous samples with three particle sizes, therefore different convective boiling heat transfer performances were obtained.

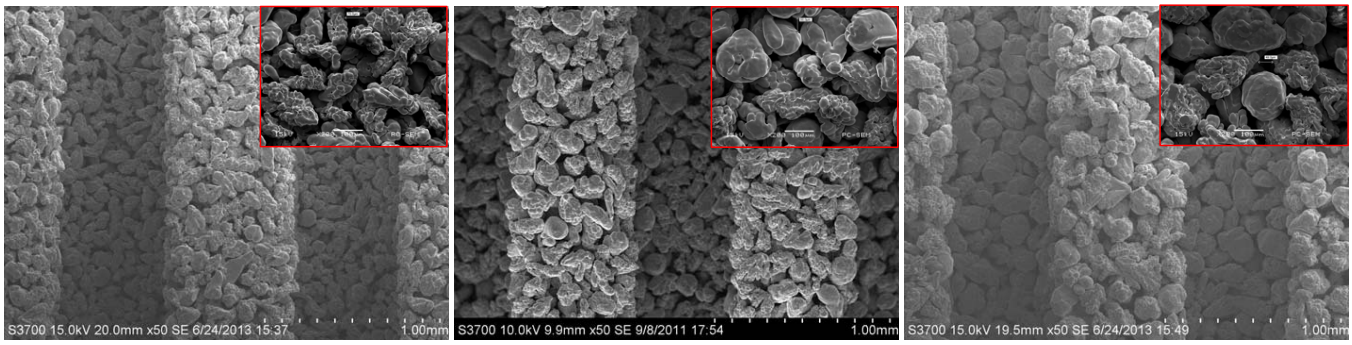

(*a*) (*b*) (*c*)

Figure 12. SEM images of the top view of the three reentrant porous microchannels with irregular powder. The microscope pictures were also inserted in each picture. (*a*) RPM-I1, (*b*) RPM-I2, (*c*) RPM-I3.

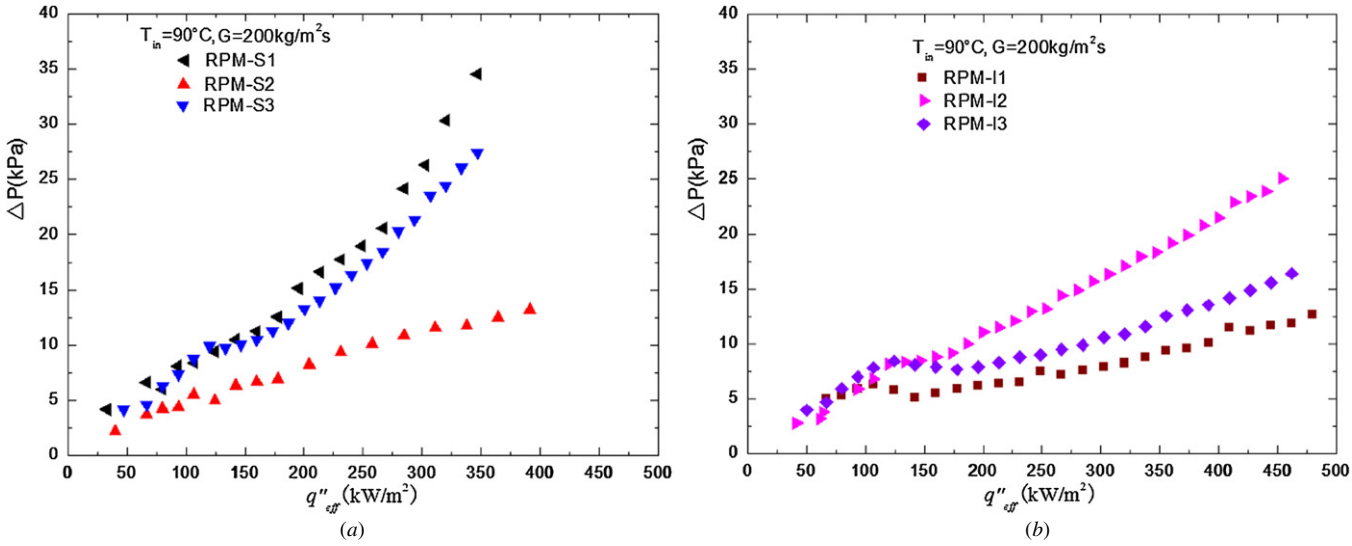

(*a*) (*b*)

Figure 13. Two-phase pressure drop of the reentrant porous microchannels: (*a*) spherical powder samples; (*b*) irregular powder samples.

4.3. Two-phase pressure drop and flow instabilities

Figure 13 shows the two-phase pressure drop characteristics as a function of efficient heat fluxes for all porous microchannels samples. With the increase of heat fluxes, the pressure drop showed an overall increasing tendency for all samples. Nevertheless, there existed a region where the ΔP changed to flatten out or drop slightly, after which it increased monotonically. This trend was especially pronounced for the three samples with irregular powder, as shown in the plots of figure 14(*b*). Such behaviors can be related to the transition of flow pattern in the microchannels as follows: firstly the bubbles flow dominated in the microchannels, which increased the gas superficial velocity and amplified the pressure drop [37]. Then, with the heat flux and vapor quality increasing, the bubbles tended to collapse together, and the bubbly flow transited to an elongated bubbly flow, in which the gas superficial velocity decreased, therefore inducing a decrease of pressure drop. Finally, with the vapor quality increasing further, the rapid annular flow governed in the microchannels, and the gas superficial velocity increased again, thus the pressure drop increased significantly. The above flow pattern transition was detailed in our previous study [23] and is not presented here again. Similar results were found during the water boiling tests on the glass microchannels by Choi *et al* [38], and the FC-77 liquid tests on the copper microchannels by Chen and Garimella [39].

For the three porous microchannel samples with spherical powder, there was no distinctive difference of ΔP for samples RPM-S1 and RPM-S3 at the early stage after the initiation of boiling. Two-phase instabilities accompanied by oscillation of the inlet pressure occurred for these two samples, as shown in figure 14(*a*). This was attributed to the rapid bubble collapse and sometimes the vapor flowed back into the inlet plenum. However, the flow reversal was not observed for sample RPM-S2, and the inlet pressure kept nearly constant even at the early stage of boiling at low heat fluxes. The pressure drop of sample RPM-S2 was also smaller than the other two samples. With the heat flux and vapor quality increasing, the ΔP of sample RPM-S1 with the smallest powder size 50–75 μm increased rapidly, and outperformed that of sample RPM-S3. It has reached a very high value (>35 kPa) when it approached to the situation of CHF. Sample RPM-S2 presented a steady and gradual increase of ΔP, and the smallest pressure drop was reached. The possible reason for the above differences of pressure drop for the three samples may be the different effects of spherical particle size on the frictional and acceleration pressure loss.

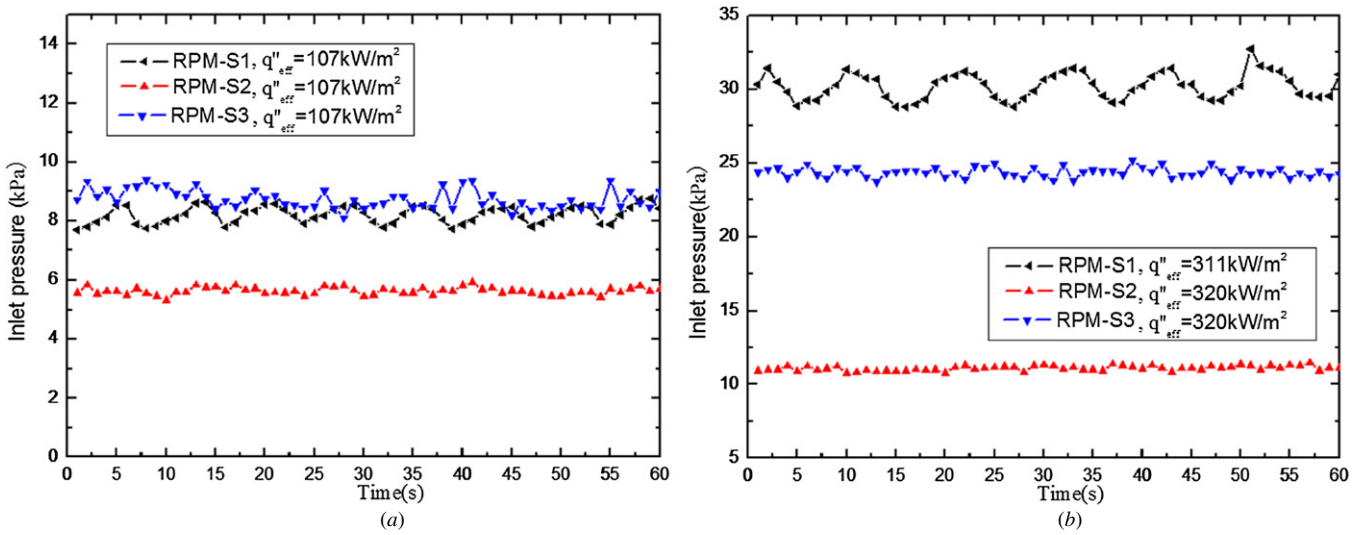

Figure 14. Variation of inlet pressure of three porous microchannel samples with spherical powder at $T_{in} = 90\ ^{\circ}\mathrm{C}$, $G = 200\ \mathrm{kg\ m^{-2} \cdot s^{-1}}$: (*a*) low heat flux; (*b*) high heat flux.

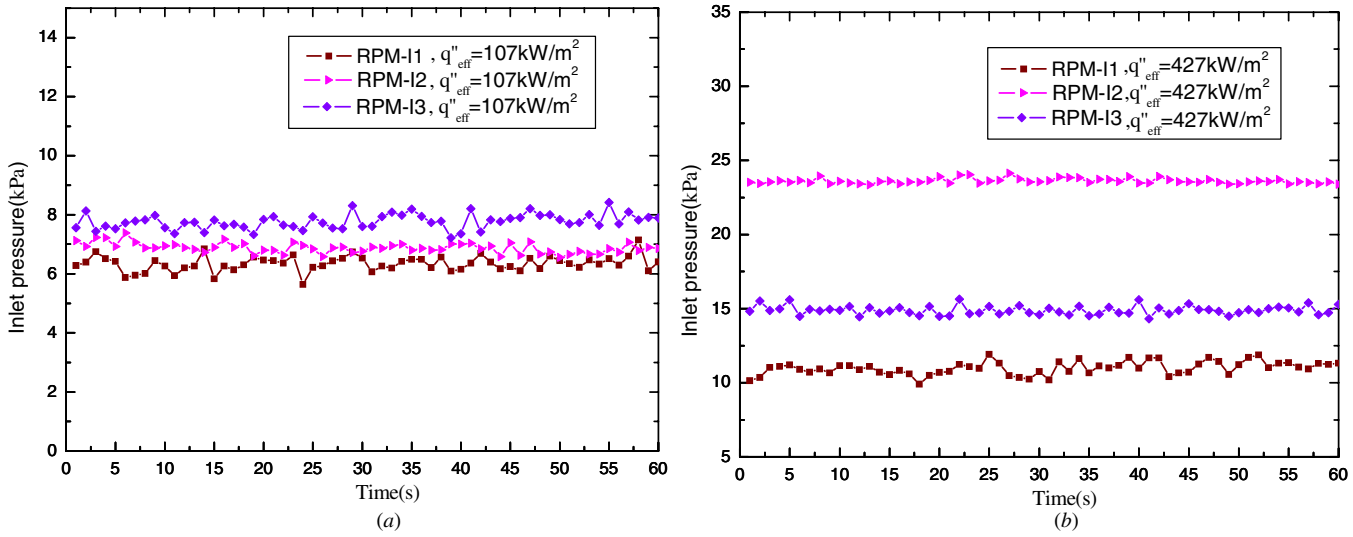

Figure 15. Variation of inlet pressure of three porous microchannel samples with irregular powder at $T_{in} = 90\ ^{\circ}\mathrm{C}$, $G = 200\ \mathrm{kg\ m^{-2} \cdot s^{-1}}$: (*a*) low heat flux; (*b*) high heat flux.

For sample RPM-S1, as the small particles bonded together densely, and the pores between different particles were small and tended to close, the liquid and vapor phase were hard to penetrate into the wall surface and can only flow directly along the microchannels, therefore it facilitate the rapid flow in the microchannels, which may increase the acceleration pressure loss significantly. While for the sample RPM-S3, the large variation of protrusion and valleys in the microchannel wall due to the large particle size may increase the turbulence and shear stress notably and thus increase the frictional resistance. It also presented a large pressure drop. Sample RPM-S2 with the medium particle size may have reached a good balance of both frictional and acceleration pressure loss, therefore the smallest ΔP was obtained. Besides, as can be seen in figure 14(*b*), periodic boiling persisted even at high heat fluxes for sample RPM-S1. On the other hand, for the other two samples with larger powder size, stable boiling lasted for a long time, and the fluctuation of pressure drop was mitigated or absent at moderate to high heat fluxes. Therefore, for the spherical samples, it seems that the porous microchannel with large powder size can facilitate to maintain a steadier boiling behavior.

For the porous samples with irregular powder, during the early stage of boiling, the pressure drop differences among the three porous microchannel samples were insignificant. Slight flow instabilities occurred for all three samples, as shown in figure 15(*a*). However, with the increase of heat flux and vapor quality, the pressure drop of three samples diverged to increase differently, indicating that the particle size played a dominant role on the pressure drop. Sample RPM-I2 with the intermediated size of 75–110 μm produced the largest pressure drop, and the smallest one was reached by sample RPM-I1 with the smallest particle size. As mentioned before, the annular flow dominated in the porous microchannel at this stage. The vapor core flowed in the center of the microchannel, while the liquid thin film existed in the periphery of microchannel wall.

The wall surface may play an important role on the liquid film, i.e., a rougher surface leads to an earlier breakage of the liquid film [40]. The broken and dispersed liquid film in the rougher microchannels may result in an increase of two-phase pressure drop. Therefore, with the surface roughness increased, the pressure drop of RPMs with irregular powder tended to become larger. Nevertheless, two-phase flow instabilities were found to be suppressed for sample RPM-I2, as shown in figure 15(*b*), while the small amplitude of fluctuation of inlet pressure still existed for sample RPM-I1 and RPM-I3. This indicated that RPM-I2 was favorable for mitigating flow instabilities. Recognizing that RPM-I2 has the largest surface roughness, as shown in table 2, it seems that the rough surface can promote the stability of two-phase flow. This can be explained by the fact that a rough surface can trigger a rapid transition from bubbly flow to annular flow [41], thereby reducing the instabilities caused by the rapid bubble formation and collapse. It should be mentioned that the wall roughness only plays a role in the pressure drop and flow instability behavior of the irregular porous samples, but not the spherical samples. This may be due to the smooth particle surface and uniform packing characteristics of spherical samples, and the roughness may exert a less predominant role on the liquid film during the convective boiling.

4.4. Evaluation of optimum design

By the combination of both heat transfer performance and pressure drop, one can note that, for the spherical samples, sample RPM-S1 performed worst in both heat transfer and pressure drop. Though the sample RPM-S3 exhibited the largest heat transfer performance, it needed large pump power due to high pressure drop, which may hinder its application in heat sink cooling. Sample RPM-S2 produced the smallest pressure drop and medium heat transfer performance. Meanwhile, it showed its excellent superiority in the mitigation of the detrimental two-phase instabilities. Therefore, it seems to be the optimum choice in these three porous microchannel samples. While for the three samples with irregular powders, it can be found that the largest h_{tp} and smallest ΔP can be obtained by sample RPM-I1, despite the slight two-phase instabilities accompanying the boiling flow. Moreover, sample RPM-I1 also produced a better heat transfer performance and smaller pressure drop than any of the samples with spherical samples. Therefore, it seems that irregular powder with size of 50–75 μm should be selected for the irregular porous samples to achieve the highest performance in the cooling of high heat-flux microelectronics chips.

5. Conclusions

In summary, a series of porous microchannels with the Ω shape were fabricated for heat sink cooling by the solid-state sintering method with the aid of specially designed sintering replication modules. Micro wire EDM was utilized to process the modules, and the machinability of the graphite module by micro EDM was demonstrated. The surface roughness characteristics of these porous microchannels were examined. The dependence of flow boiling performance, i.e., two-phase heat transfer, pressure drop and flow instabilities, on the copper powder type and size were accessed. These porous microchannels were found to reduce the wall superheat for the onset of nucleate boiling significantly. The two-phase heat transfer performance was enhanced with the increase of particle size for the porous microchannels with spherical powder, while an inverse trend existed for the samples with irregular powder. For the spherical samples, the porous microchannels with large powder size facilitated a steady boiling behavior to be maintained, and their two-phase pressure drop was also smaller than the one with the smallest particle size, 50–75 μm. The pressure drop of the porous microchannel with irregular powder was believed to depend on the wall surface roughness. In the present experimental range, the irregular powder with the smallest size of 50–75 μm was considered to be the optimum one to construct the porous microchannel heat sinks to achieve the highest performance for the cooling of high heat-flux microelectronic chips.

Acknowledgments

The research was financially supported under the grants of the National Nature Science Foundation of China No. 51275180 and the National Nature Science Foundation of Guangdong Province No. S2012030006231.

References

[1] Tuckerman D B and Pease R F W 1981 High-performance heat sinking for VlSI *IEEE Electron Device Lett.* **2** 126–9
[2] Agostini B, Fabbri M, Park J E, Wojtan L, Thome J R and Michel B 2007 State of the art of high heat flux fooling technologies *Heat Transfer Eng.* **28** 258–81
[3] Lee M, Wong Y Y, Wong M and Zohar Y 2003 Size and shape effects on two-phase flow patterns in microchannel forced convection boiling *J. Micromech. Microeng.* **13** 155–64
[4] Wu H Y, Cheng P and Wang H 2006 Pressure drop and flow boiling instabilities in silicon microchannel heat sinks *J. Micromech. Microeng.* **16** 2138–46
[5] Liu G, Xu J, Yang Y and Zhang W 2010 Active control of flow and heat transfer in silicon microchannels *J. Micromech. Microeng.* **20** 045006
[6] Joo Y, Yeh H T, Dieu K and Kim C 2008 Air cooling of a microelectronic chip with diverging metal microchannels monolithically processed using a single mask *J. Micromech. Microeng.* **18** 115022
[7] Mei F, Phillips W A, Lu B, Meng W J and Guo S 2009 Fabrication of copper-based microchannel devices and analysis of their flow and heat transfer characteristics *J. Micromech. Microeng.* **19** 035009
[8] Sommers A D and Yerkes K L 2013 Using micro-structural surface features to enhance the convective flow boiling heat transfer of R-134a on aluminum *Int. J. Heat Mass Transfer* **64** 1053–63
[9] Ammerman C N and You S M 2001 Enhancing small-channel convective boiling performance using a microporous surface coating *ASME J. Heat Transfer* **123** 976–83
[10] Khanikar V, Mudawar I and Fisher T 2009 Effects of carbon nanotube coating on flow boiling in a micro-channel *Int. J. Heat Mass Transfer* **52** 3805–17
[11] Wang H and Peterson R B 2010 Enhanced boiling heat transfer in parallel microchannels with diffusion brazed wire mesh *IEEE Trans. Compon. Packag. Technol.* **33** 784–93

[12] Sun Y, Zhang L, Xu H and Zhong X 2011 Subcooled flow boiling heat transfer from microporous surfaces in a small channel *Int. J. Therm. Sci.* **50** 881–9
[13] Hakamada M, Asao Y, Saito N and Mabuchi M 2008 Microfluidic flows in metallic microchannels fabricated by the spacer method *J. Micromech. Microeng.* **18** 075029
[14] Cora O N, Usta Y and Koc M 2009 Micro-manufacturing of micro-scale porous surface structures for enhanced heat transfer applications: an experimental process optimization study *J. Micromech. Microeng.* **19** 045011
[15] Cora O N, Min D, Koc M and Kaviany M 2010 Microscale-modulated porous coatings fabrication and pool-boiling heat transfer performance *J. Micromech. Microeng.* **20** 035020
[16] Benjamin J E and Westwater J W 1961 Bubble growth in nucleate boiling of binary mixture *Int. development in heat transfer (New York)* pp 212–8
[17] Chien L H and Webb R L 1998 Visualization of pool boiling on enhanced surfaces *Exp. Therm. Fluid Sci.* **16** 332–41
[18] Chen Y, Groll M, Mertz R and Kulenovic R 2005 Visualization and mechanisms of pool boiling of propane, isobutane and their mixtures on enhanced tubes with reentrant channels *Int. J. Heat Mass Transfer* **48** 2516–28
[19] Bergles A E 2002 ExHFT for fourth generation heat transfer technology *Exp. Therm. Fluid Sci.* **26** 335–44
[20] Goyal A, Jaeger R C, Bhavnani S H, Phadke N K, Azimi-Rashti M and Goodling J S 1993 Formation of silicon reentrant cavity heat sinks using anisotropic etching and direct wafer bonding *IEEE Electron Device Lett.* **14** 29–32
[21] de Boer M J, Tjerkstra R W, Berenschot J W, Jansen H V, Burger G J, Gardeniers J G E, Elwenspoek M and van den Berg A 2000 Micromachining of buried micro channels in silicon *J. Microelectromech. Syst.* **9** 94–103
[22] Kuo C J and Peles Y 2007 Local measurement of flow boiling in structured surface microchannels *Int. J. Heat Mass Transfer* **50** 4513–26
[23] Deng D, Tang Y, Liang D, He H and Yang S 2014 Flow boiling characteristics in porous heat sink with reentrant microchannels *Int. J. Heat Mass Transfer* **70** 463–77
[24] Wu W, Du J H, Hu X J and Wang B X 2002 Pool boiling heat transfer and simplified one-dimensional model for prediction on coated porous surfaces with vapor channels *Int. J. Heat Mass Transfer* **45** 1117–25
[25] Weibel J A, Garimella S V and North M T 2010 Characterization of evaporation and boiling from sintered powder wicks fed by capillary action *Int. J. Heat Mass Transfer* **53** 4204–15
[26] Hong F J, Cheng P, Wu H Y and Sun Z 2013 Evaporation/boiling heat transfer on capillary feed copper particle sintered porous wick at reduced pressure *Int. J. Heat Mass Transfer* **63** 389–400
[27] Peterson G P and Chang C S 1998 Two-Phase heat dissipation utilizing porous-channels of high-conductivity material *ASME J. Heat Transfer* **120** 243–52
[28] Sun Y, Zhang L, Xu H and Zhong X 2011 Flow boiling enhancement of FC-72 from microporous surfaces in minichannels *Exp. Therm. Fluid Sci.* **35** 1418–26
[29] Bai P, Tang T and Tang B 2013 Enhanced flow boiling in parallel microchannels with metallic porous coating *Appl. Therm. Eng.* **58** 291–7
[30] Sarwar M S, Jeong Y H and Chang S H 2007 Subcooled flow boiling CHF enhancement with porous surface coatings *Int. J. Heat Mass Transfer* **50** 3649–57
[31] Jones B J and Garimella S V 2009 Surface roughness effects on flow boiling in microchannels *ASME J. Heat Transfer* **1** 041007
[32] Young P L, Brackbill T P and Kandlikar S G 2009 Comparison of roughness parameters for various microchannel surfaces in single-phase flow applications *Heat Transfer Eng.* **30** 78–90
[33] Qu W and Mudawar I 2003 Measurement and prediction of pressure drop in two-phase micro-channel heat sinks *Int. J. Heat Mass Transfer* **46** 2737–53
[34] Taylor J R 1997 *An Introduction to Error Analysis* (Mill Valley, CA: University Science Books)
[35] Qu W and Mudawar I 2003 Flow boiling heat transfer in two-phase micro-channel heat sinks—I. Experimental investigation and assessment of correlation methods *Int. J. Heat Mass Transfer* **46** 2755–71
[36] Zhang L, Wang E N, Goodson K E and Kenny T W 2005 Phase change phenomena in silicon microchannels *Int. J. Heat Mass Transfer* **48** 1572–82
[37] Choi C W, Yu D I and Kim M H 2011 Adiabatic two-phase flow in rectangular microchannels with different aspect ratios. Part I: flow pattern, pressure drop and void fraction *Int. J. Heat Mass Transfer* **54** 616–24
[38] Choi C W, Shin J S, Yu D I and Kim M H 2011 Flow boiling behaviors in hydrophilic and hydrophobic microchannels *Exp. Therm. Fluid Sci.* **35** 816–24
[39] Chen T and Garimella S V 2006 Effects of dissolved air on subcooled flow boiling of a dielectric coolant in a microchannel heat sink *ASME J. Heat Transfer* **128** 398–404
[40] Thome J R, Dupont V and Jacobi A M 2004 Heat transfer model for evaporation in microchannels. Part I: presentation of the model *Int. J. Heat Mass Transfer* **47** 3375–85
[41] Bhide R R, Singh S G, Sridharan A, Duttagupta S P and Agrawal A 2009 Pressure drop and heat transfer characteristics of boiling water in sub-hundred micron channel *Exp. Therm. Fluid Sci.* **33** 963–75